Appl. Phys. A 76, 527–532 (2003)
DOI: 10.1007/s00339-002-1539-9

Applied Physics A
Materials Science & Processing

R.L.D. WHITBY[1]
W.K. HSU[1]
C.B. BOOTHROYD[2]
K.S. BRIGATTI[1]
H.W. KROTO[1]
D.R.M. WALTON[1,✉]

WS_2 layer formation on multi-walled carbon nanotubes

[1] School of Chemistry, Physics and Environmental Science, University of Sussex, Brighton, BN1 9QJ, UK
[2] Department of Materials Science & Metallurgy, University of Cambridge, Pembroke Street, Cambridge, CB2 3QZ, UK

Received: 17 June 2002/Accepted: 19 June 2002
Published online: 15 January 2003 •

ABSTRACT Time-dependent powder X-ray-diffraction analyses reveal that the conversion of WO_3 into WS_2 on carbon nanotube surfaces in the presence of H_2S is a one-step process. The WS_2 layers grow simultaneously along the tube in the radial and axial directions.

PACS 61.10.Nz; 61.46.+w; 61.50.Ks; 81.07.De; 81.10.Aj

1 Introduction

The production of WS_2 nanotubes and nanoparticles, first achieved by heating WO_3 nanoparticles at 800–1000 °C in the presence of H_2/H_2S (sulphidisation) [1], has recently been extended to WO_{3-x} and WC precursors [2–4]. X-ray-diffraction (XRD) studies, coupled with high-resolution transmission electron microscopy (HRTEM), have shown that the WO_3 particle surface is first reduced to WO_{3-x} ($x = 1$ and 2), followed by conversion into hexagonal layered WS_2 [3, 5]. The reactant gases (H_2 and H_2S) diffuse through the lattice defects in the outer WS_2 layers in order to continue the $WO_3 \rightarrow WO_{3-x} \rightarrow WS_2$ process. This 'inward' sequential layer growth process is terminated when the core is fully converted into WS_2. The morphology of the precursor essentially determines that of the product, i.e. a template effect operates [5]. The diffusion of H_2 and H_2O through defects in the formed WS_2 layer is a slow process, which requires extended periods of sulphidisation in order to complete the $WO_3 \rightarrow WS_2$ conversion. Residual WO_{3-x} is always present in the product, as revealed by powder XRD analysis [2].

Sloan et al. showed that, by annealing $WO_{(2.5-2.9)}$ nanorods in the presence of H_2/H_2S, other reduced tungsten oxide phases may also be generated and encapsulated within WS_2 particles [6]. HRTEM revealed that the tungsten oxide particle surfaces were converted into layered WS_2, and that WO_{3-x} crystalline lattice fringes were present within the core, together with numerous crystallographic shear planes and voids between the WO_{3-x} core and the outer WS_2 layers.

Recently, we produced WS_2-coated multi-walled carbon nanotubes (MWCNs) [7]. HRTEM analyses indicated that the 'inward' growth mechanism is in competition with an 'outward' growth mechanism on the MWCN surfaces. The 'outward' process is presumably facilitated by facile diffusion of H_2S through the thin and highly defective layers of WO_3 supported by the MWCNs [8]. In this paper, we probe this direct transformation of monoclinic WO_3 into hexagonal WS_2, without involving the intermediate species, i.e. WO_{3-x}.

2 Experimental

Tungstic acid (H_2WO_4, 250 mg) was mixed in liquid ammonia at −78 °C. Arc-generated MWCNs (50 mg) were added and the mixture was allowed to attain room temperature. The production of WS_2-coated MWCNs was carried out in three stages. Stage I: the solid residue, remaining after the excess of liquid ammonia had evaporated, was heated at 350 °C for 15 min in an air flow (100 $cm^3\,min^{-1}$), in order to convert the H_2WO_4 into WO_3. Stage II: the mixture was annealed at 900 °C under a N_2 flow (50 $cm^3\,min^{-1}$) for 15 min. Stage III: H_2S gas (10 $cm^3\,min^{-1}$) was then introduced at 30-s intervals per min for a total of 6 min. The solid residue was then subjected to HRTEM (Philips CM200 and JEOL 4000EX-II) and powder XRD (Siemens Diffractometer D5000, Cu $K_\alpha = 1.5418$ Å).

3 Results and discussion

3.1 *Stage I – amorphous* WO_3*-coated MWCNs*

The WO_3-coated MWCNs were heated at 350 °C in an air flow for 15 min, prior to sulphidisation. A typical example of the product is shown in Fig. 1a. The coating appears to be amorphous and is unevenly distributed over the surface of the MWCNs. Difficulties in distinguishing between the MWCN surface and the amorphous coating may have been exacerbated by the loss of the WO_3 coating during TEM operation. It is noteworthy that the arc-generated MWCNs are often coated with amorphous carbon. Our MWCN sample was annealed at 350 °C for 15 min in air, in order to remove the amorphous carbon coating [9]. Accordingly, the MWCN surface should be coated with WO_3, as confirmed by energy dispersive X-ray (EDX) spectra (see below). HRTEM showed that the WO_3 coating varies in thickness (from 0 to 2 nm) along the MWCN surface, and that the inner-core structure of coated MWCNs is still visible (Fig. 1a, arrow). Large

✉ Fax: +44-1273/677-196, E-mail: d.walton@sussex.ac.uk

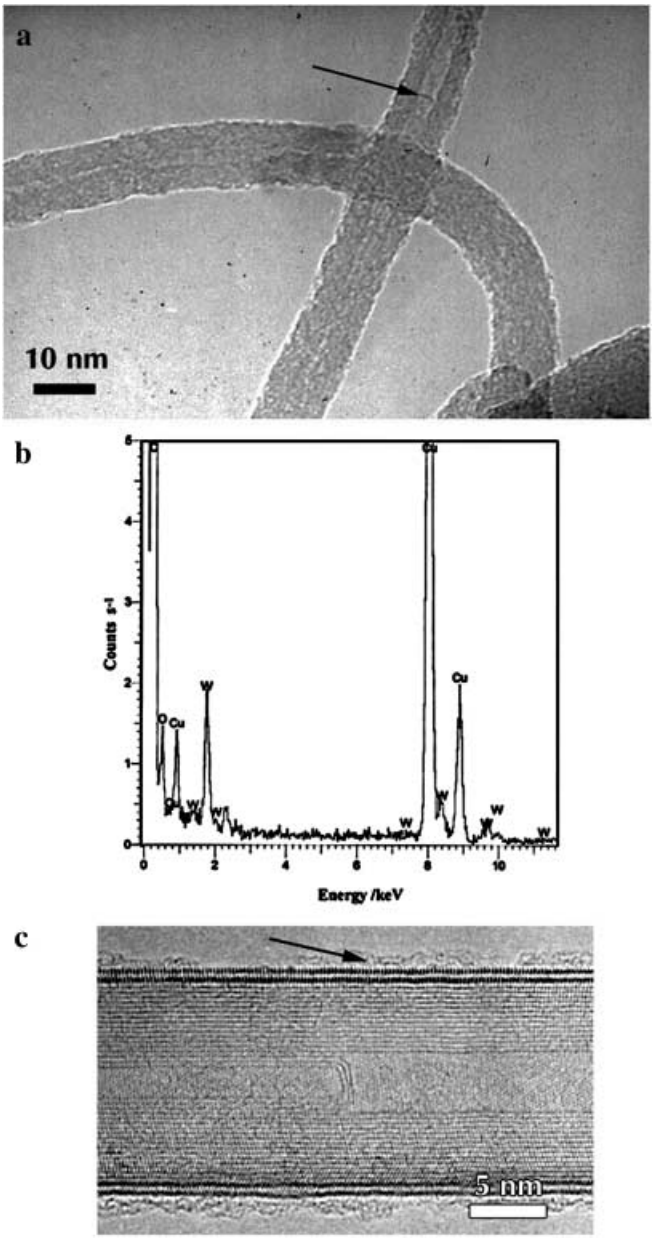

FIGURE 1 **a** TEM image of WO_3-coated MWCNs. Arrow highlights the hollow MWCN structure. **b** EDX profile of a WO_3-coated MWCN. **c** HRTEM image of a double-layered WS_2-coated MWCN. Arrow indicates amorphous WO_3 or WO_{3-x} coating

carbon particles also exhibited similar amorphous coatings. EDX analyses were conducted on both coated and uncoated MWCNs. The uncoated MWCNs showed only the C signal, whereas coated MWCNs showed C, W and O signals (Fig. 1b). The thickness of the WO_3 coating facilitates formation of up to two WS_2 layers on the MWCN surface, assuming a $\sim$ 6.2-Å d spacing along the c axis for WS_2 and a $\sim$ 4.4-Å separation between the innermost WS_2 layer and the outermost carbon layer [7].

XRD analysis of the WO_3-coated MWCNs annealed at 350 °C revealed the presence of several small reflections (Fig. 2a), which makes the assignment of a crystal system to WO_3 difficult. However, the peaks which appear at low angles are correlated with monoclinic lattice arrays and are present in

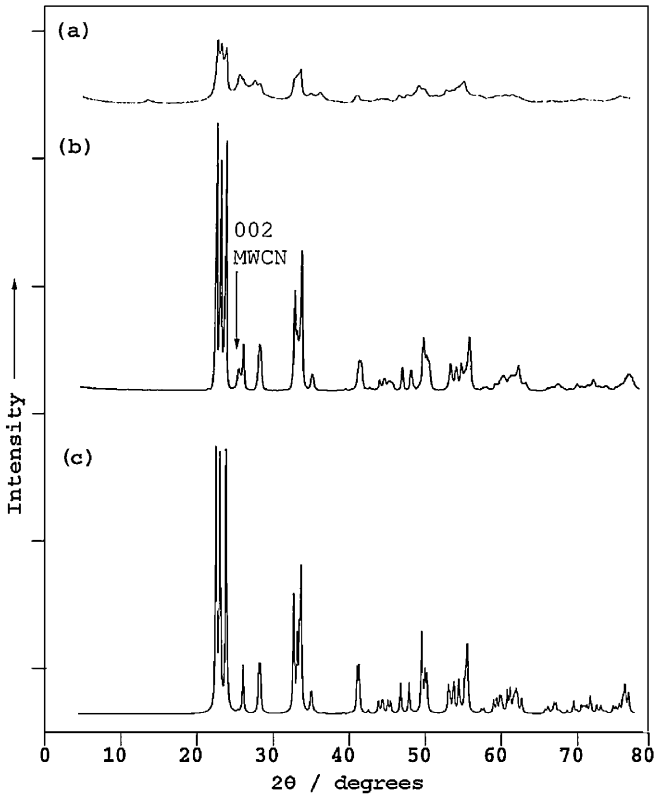

FIGURE 2 XRD profiles of **a** 300 °C annealed WO_3-coated MWCNs and **b** 900 °C annealed WO_3-coated MWCNs. **c** Simulated XRD profile for monoclinic WO_3

a predominantly amorphous sample; the 002 reflection, arising from MWCNs at $\sim 2\theta = 26.5°$ (i.e. a value similar to that previously reported for pure MWCNs) [10], overlaps slightly with WO_3.

3.2 *Stage II – annealed* WO_3*-coated MWCNs*

Amorphous WO_3-coated MWCNs were annealed at 900 °C under N_2 for 15 min. At this stage the resulting solid contains WO_3-coated MWCNs, bare MWCNs and WO_3 particles. The XRD profile of annealed WO_3-coated MWCNs (Fig. 2b) shows that the WO_3 reflections mostly overlap with MWCNs. The only visible peak for MWCNs is the 002 reflection at $\sim 2\theta = 26.5°$ (Fig. 2b, arrow). XRD indicates that the WO_3 structure has a well-defined monoclinic phase; reflection intensities are much stronger than those of stage I and match the computer-simulated powder XRD pattern of a WO_3 monoclinic crystal (Fig. 2c) [11]. However, HRTEM failed to reveal distinct lattice fringes for WO_3 coating the MWCNs (previously observed in pure WO_3 nanocrystals) [6], possibly for the following reasons. First, the MWCN lattice fringes interfere with WO_3. Secondly, the crystal growth on a planar substrate is linear with respect to the $x-y$ and $y-z$ planes. The MWCN surface is curved, implying that the stacking of W and O atoms to form crystal structures can only be achieved locally on the MWCN surface. If the localised WO_3 crystal domains are not well aligned to the incident beam, or are covered by amorphous WO_3, distinct WO_3 lattice fringes will not emerge. Meanwhile, determination by HRTEM of the

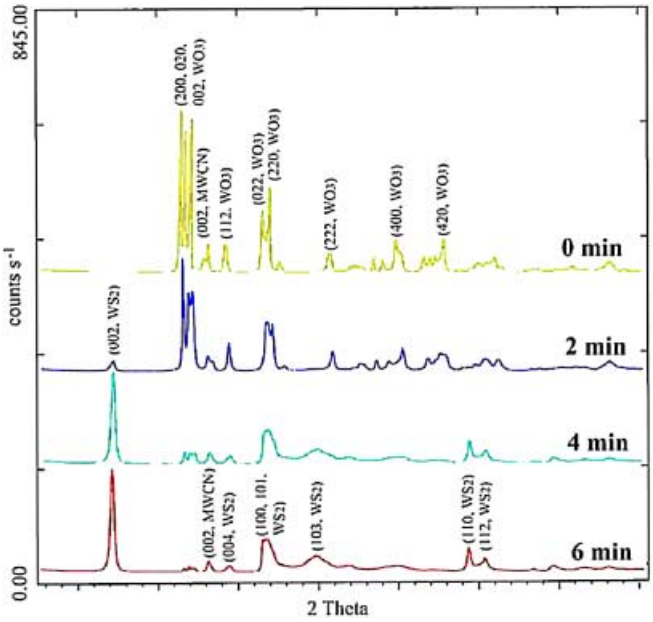

FIGURE 3 XRD profiles of sulphidisation at 0-, 2-, 4- and 6-min intervals

spacing between the WO_3 and the MWCN surface is difficult. As thin crystal layers would broaden reflection peaks, it is therefore possible that the X-ray-diffracting domains mainly arise from WO_3 particles, with a smaller contribution originating from the WO_3 coating the MWCNs. This contention is supported by the presence of three sharp reflections at low angles $2\theta = 22–24°$, i.e. a larger spacing between adjacent crystal planes along the 200, 020 and 002 directions (see Fig. 3). However, no other types of WO_3 crystal (e.g. hexagonal phase) were found in XRD profiles, which means that the annealing of H_2WO_4 leads preferentially to a monoclinic WO_3 phase.

3.3 *Stage III – sulphidised* WO_3*-coated MWCNs*

The annealed WO_3-coated MWCNs were heated at 900 °C in the presence of H_2S/N_2 (flow rate 100 $cm^3\ min^{-1}$; $H_2S : N_2$ ratio $\sim 1 : 4$), with intervals up to a total H_2S exposure time of 6 min. The XRD graphs of 0-, 2-, 4- and 6-min sulphidisation periods are displayed in Fig. 3, in which the major reflections due to WO_3, WS_2 and MWCN are labelled.

3.3.1 2-min *sulphidisation (Fig. 3).* As a result of 2-min sulphidisation, the intensities of all WO_3 reflections are reduced by $\sim 20\%$. A small peak, corresponding to 002 reflections of WS_2, is present at this stage, implying that H_2S has begun to replace O atoms by S in the WO_3 coating and particles. Surface substitution of O by S will result in the presence of partial oxygen vacancies in the lattice arrays, and thence to maintenance of a monoclinic system with low-intensity peaks [6]. This outcome is consistent with the concept that the type of crystal lattice determines the peak distribution and that the atomic arrangement determines the reflection intensity [12].

3.3.2 4-min *sulphidisation (Fig. 3).* The WO_3 reflections 002, 020, 200 and 222 decreased to $\sim 20\%$ of their original intensity, whereas the WS_2 002 reflection intensities were ~ 10 times stronger than those associated with 2-min sulphidisation (blue). Due to overlap with the 100 and 101 WS_2 peaks, the extent of the intensity decrease in the 220 and 022 WO_3 peaks is unclear. A similar situation occurs for the 112 WO_3 peak. Other WS_2 peaks, including 103, 110 and 112, have become visible. The 002 MWCN peak remains unchanged.

3.3.3 6-min *sulphidisation (Fig. 3).* The WO_3 reflections are reduced to $\sim 5\%$ of their original intensity. The thin defective WO_3 coating allows H_2S diffusion and would therefore facilitate transformation into WS_2. The peaks corresponding to the remaining WO_3 could also arise from separate WO_3 structures in the sample, which can still be detected after 10-min sulphidisation. However, the XRD reflections are now predominantly WS_2, which exhibits a well-defined crystal structure. The WS_2 peak intensities and positions are strong and consistent with those of pure WS_2 nanotubes [2]. According to HRTEM investigations, $\sim 1–5$ WS_2 layers coat the MWCNs (i.e. L_c is $\sim 3–4$ nm), which is smaller than the number found in separate WS_2 particles (> 7). Therefore, the contribution to XRD profiles mainly arises from the separate WS_2 nanostructures; only a small fraction of XRD originates from the WS_2 coating. TEM reveals that 70% of the MWCNs are coated, the extent of coating varying between 25% and full coverage. Figure 1c shows a double-layered WS_2-coated MWCN, in which a small amount of residual amorphous WO_3 (or WO_{3-x}) remains on the WS_2-coated surfaces (Fig. 1c, arrow). As a consequence, insufficient W or O atoms are present within the remaining oxide lattice; hence they are unable to form another WS_2 layer or to form a reduced tungsten oxide crystalline phase. Peaks, corresponding to a reduced tungsten oxide, are absent in Fig. 3.

At this stage it is difficult to see how monoclinic WO_3 can be transformed into hexagonal WS_2, because the W-atom sites in a monoclinic cell (Fig. 4, right) differ significantly from those in a hexagonal unit cell (Fig. 4, left). For example, the nearest W–W distance along the *a* and *c* axes is 0.38 nm in a monoclinic cell, whereas in a hexagonal WS_2 cell the W–W distances along the in-plane and *c* axes are 0.31 nm and 0.62 nm respectively. The W atoms undergo significant movement during the $WO_3 \rightarrow WS_2$ conversion in order to adopt sites consistent with the hexagonal layered WS_2 struc-

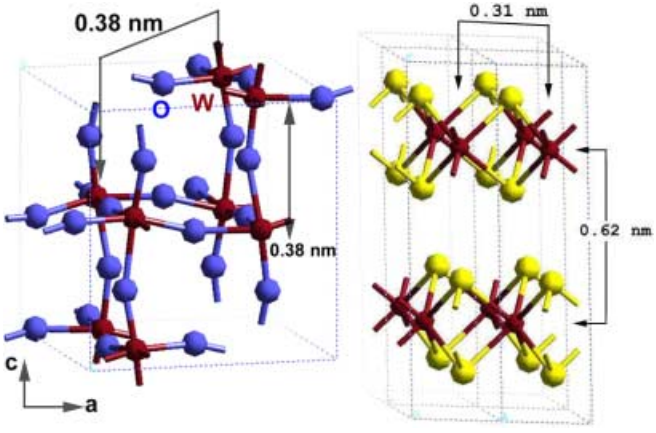

FIGURE 4 Structures of monoclinic WO_3 (*right*) and hexagonal WS_2 (*left*)

ture. Meanwhile, as WS_2 forms, the oxidation state for W in WO_3 [M^{VI} (d^0)] is reduced to M^{IV} (d^2) [13]. A previous study demonstrated that WO_3 was reduced in the initial stages of the reaction [5]. Intermediate WO_{3-x} species represent partial movement of W atoms (leading to the final structure), which have been identified by XRD and HRTEM [5, 6]. Meanwhile, W centres have been detected in pure WS_2 nanostructures, where reduction is complete [14].

Replacement of O by S in WO_3 requires a 63% lattice expansion (~ 0.24 nm) along the O–W–O (011) plane, and a 15% contraction along the (002) plane in monoclinic WO_3 ($P_{121}/n1$) respectively [11], in order to achieve the 0.62-nm (002) S–W–S basal plane spacing in WS_2 (P_{63}/mmc) (Fig. 4, right) [15]. The lattice expansion implies that a 1.5-nm-thick WO_3 coating may generate up to four WS_2 layers. The 'inward-growth' model means that the WO_3 monoclinic lattices can only expand inwards, leading to compression of the remaining inner core. This inner core compression may result in the crystallographic shear planes, reported previously by Sloan et al. [6]. In our sample, the WO_3 shear planes are not visible on the MWCN surfaces. Due to the thin defective WO_3 coating, the H_2S diffusion into the WO_3 lattice, which leads to $WO_3 \rightarrow WS_2$ conversion on the MWCN surface, most probably occurs simultaneously along the radial (Fig. 5, *c*) and axial directions (Fig. 5, *a*). The simultaneous WS_2 layer formation of WS_2 layers along both axes means that the inward compression can be minimised along the axial direction, and the need for crystallographic WO_3 shear plane formation obviated. In a previous study, we found that the WS_2 coating layers exhibited helical structures and that the WS_2 tube helicity did not correlate with MWCN lattices [7]. The absence of lattice correlation between the WS_2 coating and the MWCN surface is possibly due to the large 0.44-nm separation [7]. The WS_2 helicity is unique throughout the tube structure, as revealed by electron diffraction [7], which supports the simultaneous WS_2 layer formation along the radial and axial directions on MWCNs. If the WS_2 layer formation were achieved via the melding of localised WS_2 layered domains, the WS_2 helicity is less likely to be uniform and one might expect various sections of the WS_2 shells to exhibit a range of helicities. In order to determine the extent of WS_2 formation on MWCN surfaces, time-dependent XRD analyses were carried out on sulphidised WO_3-coated MWCNs in 30-s intervals (Fig. 6). The extent of WS_2 layer growth along the *c* axis versus reaction time is also shown (Fig. 6, inset), which was obtained from the full width at half maximum (FWHM) of the WS_2 002 peak [10]. The graph of WS_2 layer growth along the *c* axis can be divided into four regions, i.e. a (grey), b (blue), c (red) and d (green). No WS_2 was detected between 0 s and 50 s (region a), which is consistent with the real-time XRD data; i.e. no WS_2 in-plane L_a (e.g. 110, 100) and along the *c* axis L_c (e.g. 002, 103) reflections are present (Fig. 6). However, all WO_3 reflection intensities, e.g. 200, 020, 002, 022, 220, 222 and 112, decreased within the first 50 s. The WS_2 layer begins to form after 50 s, supported by the presence of a small WS_2 (002) peak (Fig. 6). Between 50 s and 120 s (i.e. region b), the intensity of WO_3 reflections continuously decreases and other WS_2 reflections are still absent. It is noteworthy that the XRD analysis shows only a slight increase

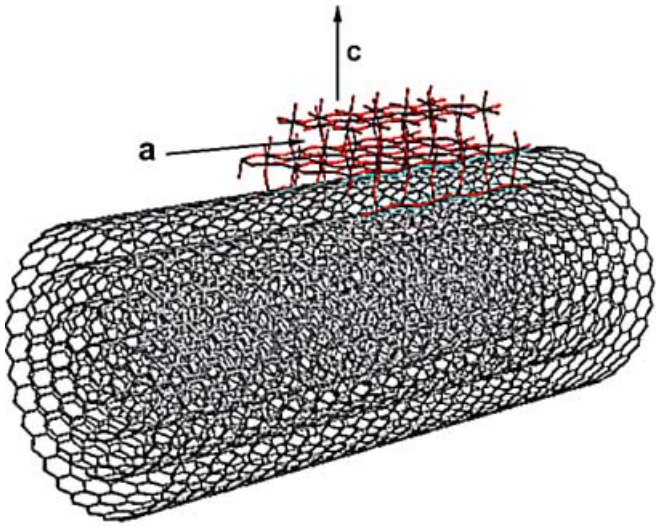

FIGURE 5 Simultaneous growth model of WS_2 layers along the carbon nanotube radial (*c*) and axial (*a*) directions

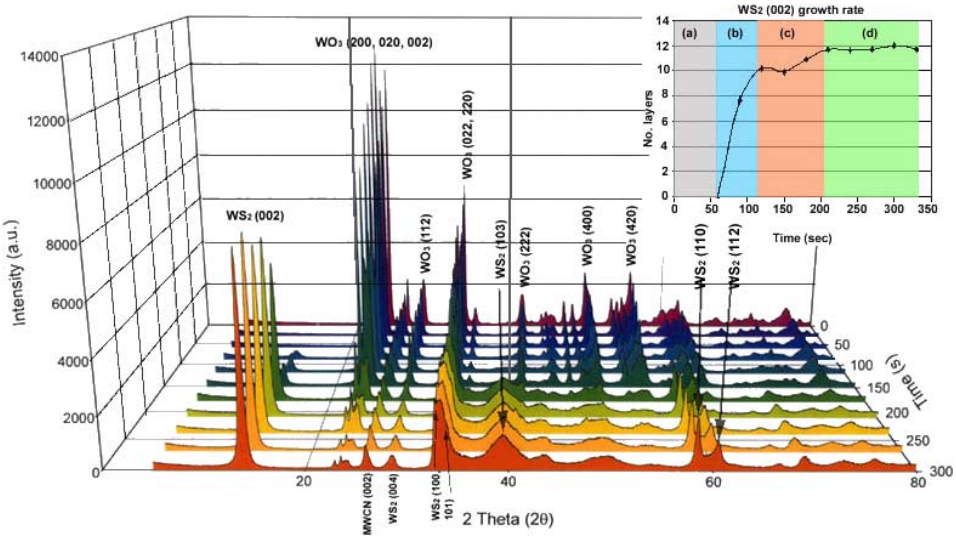

FIGURE 6 Time-dependent XRD profiles of sulphidisation in 25-s intervals (*inset*: WS_2 layer extent versus time)

in WS_2 (002) peak intensity (50–120 s, Fig. 6); however the number of WS_2 layers has already reached 10 (region b, inset). The WS_2 (002) peak intensity increases significantly in the 120–200-s range, and other WS_2 peaks, e.g. 103, 110, 100 and 112 (Fig. 6), become visible. The number of WS_2 layers within region c increases by two (inset). The intensity of all WO_3 peaks decreases significantly in region c. The peak intensity and number of WS_2 layers in region d are similar to c. Figure 6 provides useful information regarding WO_3 transformation into WS_2 on MWCN surfaces. First, region (a) corresponds to the diffusion of H_2S into defective WO_3 coating layers. In previous reports, Feldman et al. pointed out that the 1–2 WS_2 layers formed rapidly on the oxide particle surface within a few seconds, inhibiting particle aggregation [5, 16]. In our experiments, the absence of WS_2 layer formation between 0 s and 50 s (i.e. region a) is possibly due to insufficient hydrogen, i.e. the reducing agent arises only from H_2S (see Sect. 2), which slows the rate of reduction of the oxide coating. The role of H_2 during $WO_3 \rightarrow WS_2$ conversion has been described previously; it was found that an excess of H_2 is required in order to rapidly reduce WO_3 to $WO_{2.9}$ or $WO_{2.7}$ (i.e. the intermediate phase) [16]. The presence of suboxides probably facilitates WS_2 formation, because the suboxides possess octahedral structures (similar to the WS_2 structure) enabling ready replacement of O by S [16]. In our experiments, region a shows no WS_2 layer formation, but provides a longer time for H_2S diffusion into the coating WO_3, prior to $WO_3 \rightarrow WS_2$ conversion, which assists simultaneous WS_2 layer growth along the *c* (radial) and *a* (axial) directions (Fig. 5). Between 50 s and 120 s (i.e. region b), the rapid increase in the number of WS_2 layers (Fig. 6, inset) is consistent with the simultaneous WS_2 layer formation model along the *c* and *a* axes. Nevertheless, the WS_2 (002) peak intensity in region b shows only a small increase, as compared with region c (i.e. 120–200 s, Fig. 6). Meanwhile, it is noteworthy that the WS_2 002 peak width in region b remains the same as that in region c, indicating that the number of WS_2 layers on the MWCN surfaces is the same for both regions. In other words, WS_2 growth on MWCN surfaces has already ceased in region b. Previous XRD profiles, based on the inward growth model of WS_2 particles, showed that the WS_2 peak intensity increases with WO_3 peak intensity, which decreases with time [5, 16]. The increase/decrease in WS_2 and WO_3 peak intensities respectively is due to the fact that more WO_3 is converted into WS_2 layers. In our experiments, WS_2 layer formation on MWCN surfaces is rapid, which means that region b should exhibit a rapid increase/decrease in WS_2 (002) and WO_3 peak intensities respectively. However, this phenomenon is not observed. According to XRD data, the monoclinic WO_3 structure dominates in the overall sample between 50 s and 120 s (i.e. region b), mainly arising from the unreacted WO_3. The question therefore arises as to what is the actual WS_2 structure in regions b and c, because the WS_2 002 reflection exhibits the same peak width, with different intensities. The XRD intensity is determined by the type and position of the atoms within the unit cell; the larger the crystallite, the sharper the peak [12]. A small increase in WS_2 peak intensity (region b) implies that the S atoms have not yet fully occupied O vacancies, but that the host structure (monoclinic phase) has already been transformed into the hexagonal

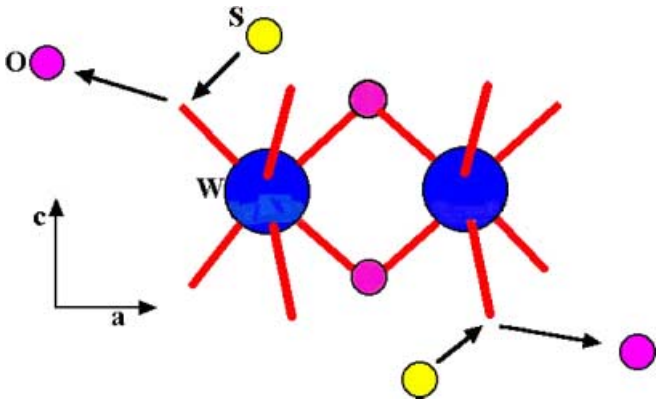

FIGURE 7 The structure of WS_2 in region b

cell. Accordingly, the XRD peaks of region b mainly arise from W atoms. As time progresses, more S atoms can occupy the lattice vacancies and the XRD peak intensity increases. Previous workers [16] proposed a structure consisting of two W-centred octahedral units connected via an O atom, with O atoms missing at the upper and lower sites of a prismatic cell. This structure provides a preferential pathway for O–S substitution about the W centres via the O–W–O planes along the b axis towards the WS_2 002 planes [13]. However, the proposed structure is based on the inward growth process. The simultaneous formation of WS_2 on MWCN surfaces provides no preferential pathway for O–S substitution, and all W atoms need to be relocated within the cell. The structure of the W/O/S in region a is complex and remains to be established. Figure 7 shows the corresponding structures of WS_2 in region b, in which adjacent W atoms are connected via O atoms, similar to the O–W–O plane along the c axis (Fig. 4, right). When O atoms are released from the lattices, the S atoms immediately occupy the vacancies. In region b, the O population is greater than that of S; more S atoms are present in the lattice as the reaction time is extended (region c). The presence of a slight increase in the WS_2 layer number in regions c and d possibly arises from other WS_2 particles, not WS_2-coated MWCNs, because the H_2S diffusion and O–S substitution can still proceed on other larger WO_3 particles.

In summary, the XRD study shows that the conversion of WO_3 into WS_2 is a one-step process. The WS_2 layers grow simultaneously along radial as well as axial directions and no intermediate phases are involved. Time-dependent XRD profiles show that the WS_2 growth on the MWCN surfaces ceases before 120 s have elapsed.

ACKNOWLEDGEMENTS We thank the Leverhulme Trust, EPSRC and the Wolfson Foundation (UK) for the financial support.

REFERENCES

1 R. Tenne, L. Margulis, M. Genut, G. Hodes: Nature **360**, 444 (1992)
2 Y.Q. Zhu, W.K. Hsu, H. Terrones, N. Grobert, B.H. Chang, M. Terrones, B.Q. Wei, H.W. Kroto, D.R.M. Walton, C.B. Boothroyd, I. Kinloch, G.Z. Chen, A.H. Windle, D.J. Fray: J. Mater. Chem. **10**, 2570 (2000)
3 Y.Q. Zhu, W.K. Hsu, N. Grobert, B.H. Chang, M. Terrones, H. Terrones, H.W. Kroto, D.R.M. Walton, B.Q. Wei: Chem. Mater. **12**, 1190 (2000)

4 A. Rothschild, J. Sloan, A.P.E. York, M.L.H. Green, J.L. Hutchison, R. Tenne: Chem. Commun. 363 (1999)
5 Y. Feldman, G.L. Frey, M. Homyonfer, V. Lyakhovitskaya, L. Margulis, H. Cohen, G. Hodes, J.L. Hutchison, R. Tenne: J. Am. Chem. Soc. **118**, 5362 (1996)
6 J. Sloan, J.L. Hutchison, R. Tenne, Y. Feldman, T. Tsirlina, M. Homyonfer: J. Solid State Chem. **144**, 100 (1999)
7 R.L.D. Whitby, W.K. Hsu, C.B. Boothroyd, P.K. Fearon, H.W. Kroto, D.R.M. Walton: Chem. Phys. Chem. **2**, 620 (2001)
8 R.L.D. Whitby, W.K. Hsu, H.W. Kroto, D.R.M. Walton, P.K. Fearon, N.C. Billingham, I. Maurin, C.B. Boothroyd, S. Firth, R.J.H. Clark, D. Collison: Chem. Mater. **14**, 2209 (2002)
9 P.M. Ajayan, T.W. Ebbesen, T. Ichihashi, S. Iijima, K. Tanigaki, H. Hirua: Nature **362**, 522 (1993)
10 W.K. Hsu, S. Firth, P. Redlich, M. Terrones, H. Terrones, Y.Q. Zhu, N. Grobert, A. Schilder, R.J.H. Clark, H.W. Kroto, D.R.M. Walton: J. Mater. Chem. **10**, 1425 (2000)
11 C.D.S.–I.C.S. Database, File 56 238, Monoclinic WO_3, accessed July (2001)
12 L.V. Azaroff, M.J. Buerger: *The Powder Method* (McGraw-Hill, New York 1958) pp. 24–26
13 W.K. Hsu, Y.Q. Zhu, C.B. Boothroyd, I. Kinloch, S. Trasobares, H. Terrones, N. Grobert, M. Terrones, R. Escudero, G.Z. Chen, C. Colliex, A.H. Windle, D.J. Fray, H.W. Kroto, D.R.M. Walton: Chem. Mater. **12**, 3541 (2000)
14 A. Rothschild, J. Sloan, R. Tenne: J. Am. Chem. Soc. **122**, 5169 (2000)
15 C.D.S.–I.C.S. Database, JCPDS 8-237, Hexagonal WS_2, accessed July (2001)
16 Y. Feldman, V. Lyakhovitskaya, R. Tenne: J. Am. Chem. Soc. **120**, 4176 (1998)